Research Square

Preprints are preliminary reports that have not undergone peer review. They should not be considered conclusive, used to inform clinical practice, or referenced by the media as validated information.

Non-equilibrium flow of dense inhomogeneous fluids in nano-channels

Baochao Shan
The University of Edinburgh
Long Ju
Harbin Engineering University
Wei Su
Hong Kong University of Science and Technology Department of Mathematics
Zhaoli Guo (zlguo@hust.edu.cn)
https://orcid.org/0000-0003-3893-6448
Yonghao Zhang
Chinese Academy of Sciences

Research

Keywords: Non-equilibrium flow, Enskog theory, Mean-field theory, Molecular dynamic simulation

Posted Date: October 24th, 2022

DOI: https://doi.org/10.21203/rs.3.rs-2167714/v1

License: This work is licensed under a Creative Commons Attribution 4.0 International License.
Read Full License

RESEARCH

Non-equilibrium flow of dense inhomogeneous fluids in nano-channels

Baochao Shan[1], Long Ju[2], Wei Su[3], Zhaoli Guo[4*] and Yonghao Zhang[5*]

*Correspondence:
zlguo@hust.edu.cn;
yonghao.zhang@imech.ac.cn
[4]Institute of Interdisciplinary Research for Mathematics and Applied Science, Huazhong University of Science and Technology, Wuhan, China
[5]Institute of Mechanics, Chinese Academy of Sciences, Beijing, China
Full list of author information is available at the end of the article

Abstract

The Enskog-Vlasov equation provides a consistent description of the microscopic molecular interactions for real fluids based on the kinetic and mean-field theories. The present fluid flows in nano-channels are investigated by the Enskog-Vlasov-BGK model, which simplifies the complicated Enskog-Vlasov collision operator and enables large-scale engineering design simulations. The density distributions of real fluids are found to exhibit inhomogeneities across the nano-channel, particularly at large densities, as a direct consequence of the inhomogeneous force distributions caused by the real fluid effects including the fluid molecules' volume exclusion and the long-range molecular attraction. In contrast to the Navier-Stokes equation with the slip boundary condition, which fails to describe nano-scale flows due to the coexistence of confinement, non-equilibrium, and real fluid effects, the Enskog-Vlasov-BGK model is found to capture these effects accurately as confirmed by the corresponding molecular dynamics simulations for low and moderate fluid densities.

Keywords: Non-equilibrium flow; Enskog theory; Mean-field theory; Molecular dynamic simulation

1 Introduction

Although significant progress has been achieved in fluid mechanics, it remains a research challenge to model real fluid flows at the nanoscale due to a plethora of underlying factors [1], which involve the fluid molecules' volume exclusion and the long-range attraction between molecules. At the macroscopic level, fluid flows can be described by the conventional continuum models such as the Navier-Stokes (NS) equations based on the mass, momentum, and energy conservations [2]. In such models, the microscopic dynamics of fluid molecules (such as the attractive and repulsive forces) are reflected by the transport coefficients, i.e. viscosity and thermal conductivity. The NS equations become invalid for non-equilibrium or strongly inhomogeneous (i.e. gas properties vary appreciably over a molecule size) fluid flows, which are frequently encountered at the nanoscale where the surface confinement effect plays a non-negligible role [3, 4]. While the density oscillation across the channel can be captured by the generalised hydrodynamic model [5], the non-equilibrium effect is better to be studied by gas kinetic theory.

The Boltzmann equation has been widely adopted to capture the non-equilibrium effect of dilute gas flows based on the assumption that the gas molecule size (σ) is negligibly smaller than the gas mean free path (λ), i.e. gas molecules are point-like with no finite spatial expansion [6, 7, 8], as shown in Figure 1(a). This assumption

is appropriate for gas flows at relatively low pressures such as aeronautics and astronautics [9], micro-electromechanical systems [10, 11], and vacuum technology [12]. The degree of the non-equilibrium can be quantified by the Knudsen number (Kn), which is defined as the ratio of the gas mean free path to the characteristic flow length(H), i.e.

$$\mathrm{Kn} = \frac{\lambda}{H}. \tag{1}$$

Based on the value of Kn, dilute gas flows can be divided into four flow regimes, i.e. continuum flow ($\mathrm{Kn} < 0.001$), slip flow ($0.001 < \mathrm{Kn} < 0.1$), transition flow ($0.1 < \mathrm{Kn} < 10$), and free molecular flow ($\mathrm{Kn} > 10$). As the gas pressure dramatically increases, e.g. natural gas development from unconventional shale gas reservoirs [13, 14, 15] and geological storage of carbon dioxide [16, 17], the size of a gas molecule becomes comparable with both the gas mean free path and the characteristic length of flowfield, as shown in Figure 1(b), consequently the real fluid and confinement effects come into play [18, 8]. The finite size of fluid molecules (i.e. the fluid volume exclusion effect) is taken into account in the Enskog theory for dense fluids [19, 20], which is more accurate than the Boltzmann equation to describe non-equilibrium flows of dense fluids [6, 7].

The finite size of fluid molecules plays its role in several folds. Firstly, the collision frequency between fluid molecules is changed. On one hand, the volume of fluid molecules reduces the available space for free streaming, hence the collision frequency is increased. On the other hand, the shielding of one molecule by another reduces the collision frequency [20]. The total change of the collision frequency is a combined effect of both factors, which can be quantified by the radial distribution function (χ) [21]. Secondly, when the fluid volume exclusion is not negligible, the momentum and energy of fluids are transferred not only during molecular motions but also through non-localised collisions between molecules [22, 23]. This modifies the transport coefficients of dense fluids [24]. The dense fluid effect caused by the change in collision frequency and non-localised collisions can be characterised by the reduced density (η) defined as the fraction of volume occupied by fluid molecules, i.e.

$$\eta = \frac{n\pi\sigma^3}{6}, \tag{2}$$

with n being the fluid number density and σ being the molecular diameter. Bird [25] pointed out that the dense fluid effect becomes non-negligible when $\delta/\sigma < 7$ with $\delta = n^{-1/3}$ being the average distance between molecules, which approximately corresponds to the reduced density $\eta > 0.0015$. Thirdly, the centre of fluid molecules can never reach the physical boundary if the fluid molecule size is considered, as shown in Figure 1(b). As a consequence, the effective flow domain is reduced by one molecular diameter [6]; this becomes particularly important in determining flow properties at the nanoscale since the reduction of the effective flow domain quantified by $1/C$ becomes comparable to the total flow path size, with C being the confinement factor, i.e.

$$C = \frac{H}{\sigma}. \tag{3}$$

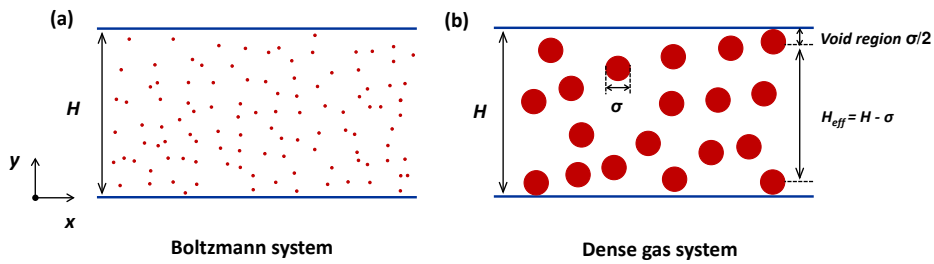

Figure 1 Schematic of confined flow systems based on (a) the dilute gas assumption and (b) dense fluid assumption.

The confinement effect arises when the confinement factor becomes small. It is noted that the confinement effect should also include the solid-fluid interaction accounting for fluid adsorption near the solid surface [26, 27, 18, 28], which is not considered in this study, since our main research focus is on the real fluid effect from fluid-fluid molecular interactions.

The original Enskog theory for dense fluids was firstly extended from the Boltzmann equation [29], where the finite size of fluid molecules is included through the modification of collision frequency and the non-localised binary collisions. In this respect, the original Enskog theory is only applicable to hardsphere fluids without considering the long-range attraction among fluid molecules. However, the importance of molecular attraction has been demonstrated in the van der Waals theory of dense fluids [30, 31], which can be modelled as a local point force by the mean-field theory. By adding a Vlasov approximation term [31] to the Enskog equation, the Enskog-Vlasov (EV) equation [32, 33] can be obtained, wherein both the fluid volume exclusion and the long-range attraction among molecules [34] are considered. It is noted here that the real fluid effect arises from both the fluid volume exclusion and the long-range attraction, while the dense fluid effect arises only from the volume exclusion.

The EV equation provides a unified description of both liquid and vapor phases. However, large-scale engineering applications of the EV equation are restricted by its formidable computational cost in evaluating the collision operator, which is in a complex integral form [35, 36]. Therefore, simplified EV model equations are proposed using the relaxation time approach [7, 37, 38, 26]. In this paper, the surface-confined flows of real fluids will be analysed by the Enskog-Vlasov-BGK (EV-BGK) model [37, 38, 26], whose accuracy will be validated by molecular dynamic (MD) simulations. The rest of the paper is organised as follows: Section 2 briefly describes the EV-BGK model and its related properties; the MD setup details are also given in this section. In Section 3, the non-equilibrium flow of real fluids is investigated by the EV-BGK model at different density, confinement, temperature, and fluid molecular attraction conditions. Section 4 summarises the main findings of the present study.

2 Problem setup and simulation techniques

The isothermal force-driven Poiseuille flows are investigated as the test cases. As shown in Figure 1, both dilute and dense fluids are confined between two parallelled plates with a separation of H, and the channel averaged density is maintained at n_{avg} for all the cases as

$$n_{avg} = \frac{1}{H}\int_0^H n(y)\,\mathrm{d}y. \tag{4}$$

Meanwhile, the system temperature is chosen to be $T = 273$ K, and the external force in the flow direction is chosen according to the flow configurations to ensure all the flows to be in the linear flow regime.

2.1 The Enskog-Vlasov-BGK model

The EV equation can be derived from the BBGKY hierarchy to describe a hard-sphere fluid under an attractive force field [31], which can be written as

$$\frac{\partial f}{\partial t} + \boldsymbol{\xi}\cdot\nabla_r f + \boldsymbol{a}\nabla_\xi f = \Omega_{hs} + \Omega_{mf}, \tag{5}$$

where $f(\boldsymbol{r},\boldsymbol{\xi},t)$ is the velocity distribution function with $\boldsymbol{r}$ being the position, $\boldsymbol{\xi}$ being the molecular velocity and t being the time; $\boldsymbol{a}$ is the acceleration rate, which is related to the external force through $\boldsymbol{a} = \boldsymbol{G}/m$ with m being the mass of a fluid molecule; and Ω_{hs} is the hardsphere collision operator, which can be expressed as

$$\begin{aligned}\Omega_{hs} =&\sigma^2 \iint \Bigg[\chi\left(\boldsymbol{r}+\frac{1}{2}\sigma\boldsymbol{k}\right) f(\boldsymbol{r},\boldsymbol{\xi'}) f_1(\boldsymbol{r}+\sigma\boldsymbol{k},\boldsymbol{\xi_1'}) \\ &- \chi\left(\boldsymbol{r}-\frac{1}{2}\sigma\boldsymbol{k}\right) f(\boldsymbol{r},\boldsymbol{\xi}) f_1(\boldsymbol{r}-\sigma\boldsymbol{k},\boldsymbol{\xi_1})\Bigg]\boldsymbol{g}\cdot\boldsymbol{k}\mathrm{d}\boldsymbol{k}\mathrm{d}\boldsymbol{\xi_1},\end{aligned} \tag{6}$$

where $\boldsymbol{k}$ is a unit vector that assigns the relative position of two molecules at the time of their impact; $\boldsymbol{g} = \boldsymbol{\xi} - \boldsymbol{\xi_1}$ is the relative velocity of two colliding molecules, with $\boldsymbol{\xi}$ and $\boldsymbol{\xi_1}$ being the molecular velocities before collisions; $\boldsymbol{\xi'}$ and $\boldsymbol{\xi_1'}$ are the post-collision molecular velocities; and Ω_{mf} is the mean-field force term to describe the fluid attraction among molecules, which can be expressed as

$$\Omega_{mf} = \frac{1}{m}\nabla\left[\int_{|\boldsymbol{r'}|>\sigma} n(\boldsymbol{r}+\boldsymbol{r'})\phi_{att}(|\boldsymbol{r'}|)\,\mathrm{d}\boldsymbol{r'}\right]\cdot\nabla_\xi f, \tag{7}$$

where ϕ_{att} the attractive potential between two molecules, i.e.

$$\phi_{att} = \begin{cases} 0, & |\boldsymbol{r'}| < \sigma, \\ -4\epsilon\left(\dfrac{\sigma}{r'}\right)^6, & |\boldsymbol{r'}| \geq \sigma. \end{cases} \tag{8}$$

Eqs. (5), (6) and (7) formulate the final form of the EV equation. However, the hardsphere collision operator Ω_{hs} is complicated and its evaluation is time-consuming, which restricts its engineering applications. Relaxation-time models

have been proposed to simplify the collision operator [38, 37, 26, 7]. Following these procedures, the Bhatnagar-Gross-Krook (BGK) model [39] is employed to represent the hard-core collision process, while the fluid volume exclusion is considered by an excess collision term. Therefore, the EV-BGK model can be written as [26, 40]

$$\frac{\partial f}{\partial t} + \boldsymbol{\xi} \cdot \nabla_r f + \boldsymbol{a} \nabla_\xi f = \Omega_0 + \Omega_{ex} + \Omega_{mf}, \tag{9}$$

where Ω_0 and Ω_{ex} are the BGK collision operator and the excess collision operator, respectively, which can be expressed as

$$\begin{aligned} \Omega_0 &= -\frac{1}{\tau}(f - f^{eq}), \\ \Omega_{ex} &= -V_0 f^{eq}(\boldsymbol{\xi} - \boldsymbol{u}) \cdot (2\boldsymbol{A}\chi + \boldsymbol{B}n). \end{aligned} \tag{10}$$

It is noted that Ω_0 and Ω_{ex} account for the hard-core collision and the fluid volume exclusion effect on collisions, respectively from a physical perspective. The Maxwellian local equilibrium distribution function f^{eq} is defined as

$$f^{eq} = n \left(\frac{m}{2\pi k_B T} \right)^{\frac{3}{2}} \exp\left[-\frac{m(\boldsymbol{\xi} - \boldsymbol{u})^2}{2k_B T} \right]. \tag{11}$$

The redial distribution function χ can be obtained from the Carnahan and Starling equation of state [41] as

$$\chi = \frac{1 - 0.5\eta}{(1-\eta)^3}, \tag{12}$$

where the reduced density η is evaluated at the local average density $\bar{n} = \int_{|\boldsymbol{r}'|<\sigma/2} \omega(\boldsymbol{r}') n(\boldsymbol{r} + \boldsymbol{r}')\, \mathrm{d}\boldsymbol{r}'$ [42], so Eq. (2) transforms into

$$\eta = 0.25 \bar{n} V_0 = \frac{\bar{n}\pi\sigma^3}{6}, \tag{13}$$

where $V_0 = 2\pi\sigma^3/3$ is the second-order virial coefficient in the virial expansion of the equation of state. In Eq.(10), $\boldsymbol{A}$ and $\boldsymbol{B}$, as proposed by Guo et al. [26] for inhomogeneous fluids, can be expressed as

$$\begin{aligned} \boldsymbol{A}(\boldsymbol{r}) &= \frac{120}{\pi\sigma^5} \int_{|\boldsymbol{r}'|<\sigma/2} \boldsymbol{r}' \bar{n}(\boldsymbol{r} + \boldsymbol{r}')\, \mathrm{d}\boldsymbol{r}', \\ \boldsymbol{B}(\boldsymbol{r}) &= \frac{120}{\pi\sigma^5} \int_{|\boldsymbol{r}'|<\sigma/2} \boldsymbol{r}' \chi(\bar{n})\, \mathrm{d}\boldsymbol{r}'. \end{aligned} \tag{14}$$

When fluid density varies slowly across the channel, the local average density is approximately equal to the fluid density, so that $\bar{n} \approx n$, and $\boldsymbol{A}$ and $\boldsymbol{B}$ reduce to

$$\boldsymbol{A} \approx \nabla n, \quad \boldsymbol{B} \approx \nabla \chi. \tag{15}$$

On the continuum level, the EV equation (5) and the EV-BGK model (9) correspond to the van der Waals-type equation of state [33, 5, 40], which can be written as

$$p = nk_BT(1 + nV_0\chi) + p^{att}, \tag{16}$$

where p^{att} is the attractive contribution to the equilibrium pressure. Therefore, the EV-type equations describe real fluid dynamics with both the repulsive and attractive forces among fluid molecules. In comparison, it is the hardsphere fluids that the original Enskog theory describes where the molecular attraction is ignored. In this paper, the real fluid flows will be investigated by the EV-BGK model, and the importance of long-range attraction will be elucidated by comparing the dynamics of real and hardsphere fluids.

2.2 Solution of the kinetic model

The EV-BGK model (9) is solved by the discrete unified gas kinetic scheme [43, 44, 45] together with the fully diffuse boundary condition [46] expressed as

$$f(\boldsymbol{r_w}, \boldsymbol{\xi_i}) = f^{eq}(n_w, \boldsymbol{u_w}, \boldsymbol{\xi_i}), \quad \boldsymbol{\xi_i} \cdot \boldsymbol{n} > 0, \tag{17}$$

where n_w is the fluid density at the wall determined by the condition that no particles go through the boundary, $\boldsymbol{u_w}$ is the velocity of a moving wall, and $\boldsymbol{n}$ is the inward unit vector normal to the wall. For the Poiseuille flow, $\boldsymbol{u_w} = 0$ since both plates are stationary.

The relaxation time τ relates to the fluid viscosity [7] through

$$\tau = \frac{\mu}{p}, \tag{18}$$

where $p = nk_BT$ is the homogeneous fluid pressure [47], and μ is the fluid viscosity determined by the Enskog theory [20] for dense fluids as

$$\mu = \mu_0 Y, \tag{19}$$

with

$$\mu_0 = 1.016\frac{5}{16\sigma^2}\sqrt{\frac{mk_BT}{\pi}} \tag{20}$$

being the fluid viscosity at atmospheric pressure, and

$$Y = \bar{n}V_0[\frac{1}{\bar{n}V_0\chi(\bar{n})} + 0.8 + 0.7614\bar{n}V_0\chi(\bar{n})] \tag{21}$$

being a correction function for fluid viscosity at high densities.

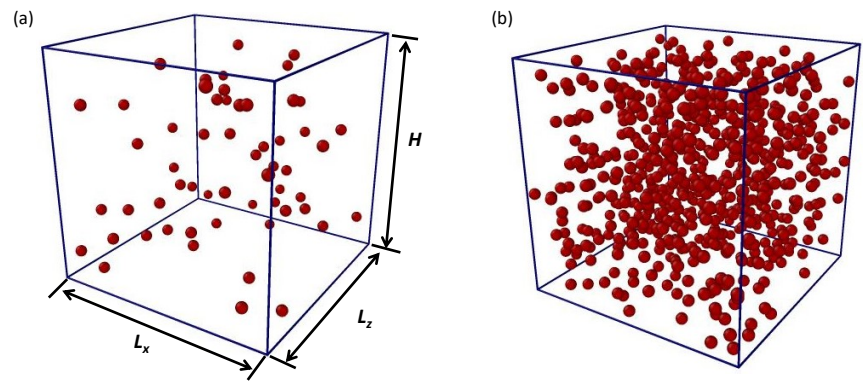

Figure 2 Schematic of the physical model in MD simulations. (a) $\rho = 30\text{kg/m}^3$, (b)$\rho = 350\text{kg/m}^3$

The macroscopic density and velocity can be determined by taking moments of the velocity distribution function as

$$\begin{aligned} n &= \int f \, \mathrm{d}\boldsymbol{\xi}, \\ n\boldsymbol{u} &= \int \boldsymbol{\xi} f \, \mathrm{d}\boldsymbol{\xi}. \end{aligned} \tag{22}$$

2.3 MD setup for surface-confined flows

MD simulations are conducted to provide benchmark data to assess the performance of the EV-BGK model (9). All simulations are run using the large-scale atomic/molecular massively parallel simulator (LAMMPS). To be consistent with the setup in the kinetic model, the number of fluid molecules N in MD is controlled by the average density n_{avg} via

$$N = n_{avg} \, L_x \, L_z \, H, \tag{23}$$

where L_x and L_z are the lengths of the physical domain in MD simulations in the x and z directions respectively, as shown in Figure 2.

The interactions among fluid molecules are described by the Lennard-Jones (LJ) potential

$$\phi_{LJ} = 4\epsilon \left[\left(\frac{\sigma}{r'} \right)^{12} - \left(\frac{\sigma}{r'} \right)^{6} \right], \quad r' < r_c, \tag{24}$$

where ϵ and σ are the energy and length parameters, and r_c is the cutoff distance, which is chosen to be $r_c = 1.2$ nm in this study.

In the MD simulations, an external force G_x is imposed on all the fluid particles along the channel (i.e. in the x direction). Periodic boundary conditions are employed in the x and z directions, while the fully diffuse boundary condition is applied to the channel walls. The system temperature is maintained at $T = 273$ K through the Nosé-Hoover thermostat. The time step is set to be 1 fs.

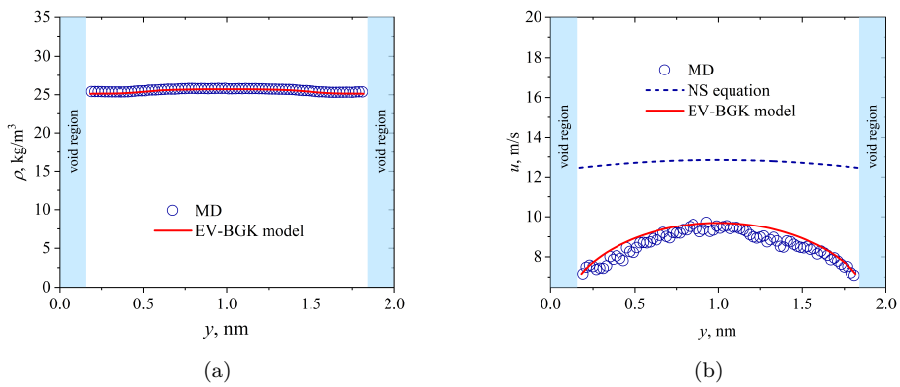

Figure 3 Density (a) and velocity (b) distributions of fluid flows in a 2-nm nanochannel with the averaged density $\rho_{avg} = 21.2$ kg/m^3.

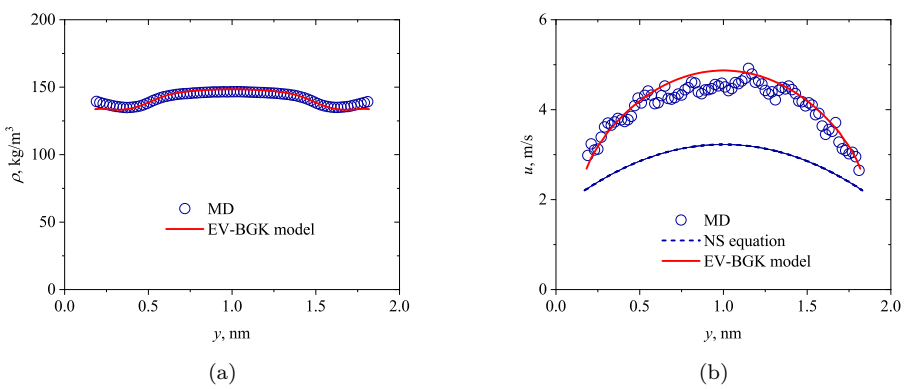

Figure 4 Density (a) and velocity (b) distributions of fluid flows in a 2-nm nanochannel with the averaged density $\rho_{avg} = 117.3$ kg/m^3.

3 Results and discussion

In this section, density and velocity distributions of surface-confined flows predicted by the EV-BGK model are compared to the MD simulation data. The density inhomogeneity arising from the real fluid effect is revealed, which is a direct result of the inhomogeneous total force distribution among fluid molecules across the channel. The effects of fluid molecular attraction and system temperature on nano-scale flows are also analysed.

3.1 Density and velocity distributions of nanoscale flows

Fluid density and velocity distributions under different density and confinement conditions are investigated in this part, with corresponding parameters summarised in Table 1. The external force G_x is chosen to ensure flows to be in the linear regime. The Knudsen number can be calculated as

$$\mathrm{Kn} = \frac{1}{\sqrt{2}n\pi\sigma^2\chi H} = \frac{1}{6\sqrt{2}\eta\chi C}, \tag{25}$$

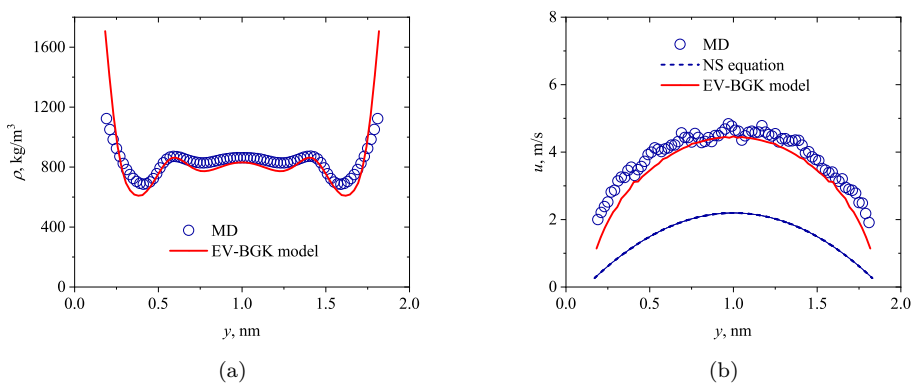

Figure 5 Density (a) and velocity (b) distributions of fluid flows in a 2-nm nanochannel with the averaged density $\rho_{avg} = 695.0$ kg/m^3.

which relates to the dense fluid effect (η) and the confinement effect (C) at the same time.

Table 1 The chosen parameters for the tested cases.

Cases	ρ, kg/^{3}	H, nm	T, K	G_x, kcal/(mol·Å)	Kn	η	H/σ
1	21.2	2	273	0.001	3.001	0.0066	5.88
2	117.3	2	273	0.0005	0.5006	0.0365	5.88
3	695.0	2	273	0.0005	0.0501	0.2163	5.88
4	8.53	5	273	0.001	3.0020	0.0027	14.69
5	49.5	5	273	0.0005	0.5010	0.0154	14.69
6	216.0	5	273	0.0003	0.1002	0.0672	14.69
7	376.0	5	273	0.0003	0.0501	0.1170	14.69
8	450.0	5	273	0.0003	0.0392	0.1400	14.69
9	695.0	5	273	0.0003	0.0200	0.2163	14.69
10	216.0	50	273	0.00003	0.0100	0.0672	146.9

The density and velocity distributions across a 2-nm nano-channel at $\rho_{avg} = 21.2$ kg/m^3, 117.3 kg/m^3 and 695.0 kg/m^3 are shown in Figures 3, 4 and 5, respectively. The fluid density ρ_{avg} relates to the fluid number density n_{avg} through $\rho_{avg} = mn_{avg}$. The fluid volume exclusion plays an important role in fluid flows under tight confinements and leads to a void region near each wall marked by the shadow in Figure 3. There is tiny density inhomogeneity when fluid density is as small as 21.2 kg/m^3, see Figure 3(a). This density inhomogeneity becomes discernible when fluid density increases to 117.3 kg/m^3 as shown in Figure 4(a) and is more significant at $\rho_{avg} = 695.0$ kg/m^3 as shown in Figure 5(a). More obvious density inhomogeneities indicate a stronger real fluid effect at higher fluid densities. Meanwhile, it is worth noting that fluid-solid interactions are not considered in this paper, so the density inhomogeneity is a direct consequence of the real fluid effect, so the density peak near the wall is not caused by fluid adsorption, see Figure 5(a) for example.

The velocity distributions predicted by the NS equation with the second-order slip boundary condition are also given as a reference of the conventional continuum theory in each case. The slip boundary condition is written as

$$u_s - u_w = \pm C_1 \lambda \left(\frac{\partial u}{\partial n}\right)_s - C_2 \lambda^2 \left(\frac{\partial^2 u}{\partial n^2}\right)_s, \tag{26}$$

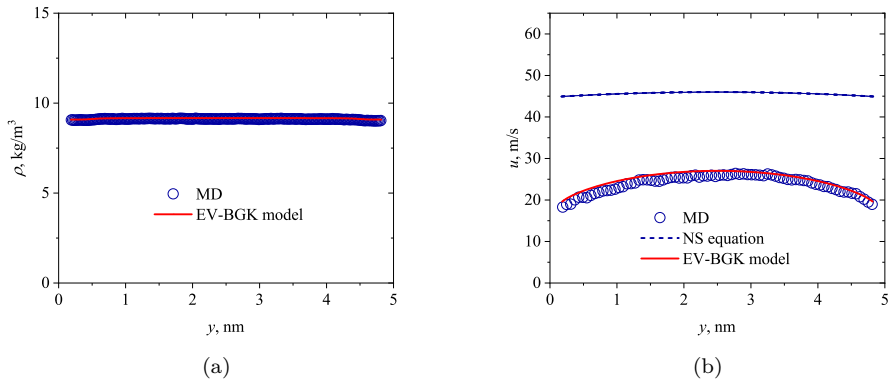

Figure 6 Density (a) and velocity (b) distributions of fluid flows in a 5-nm nanochannel with the averaged density $\rho_{avg} = 8.53$ kg/m^3.

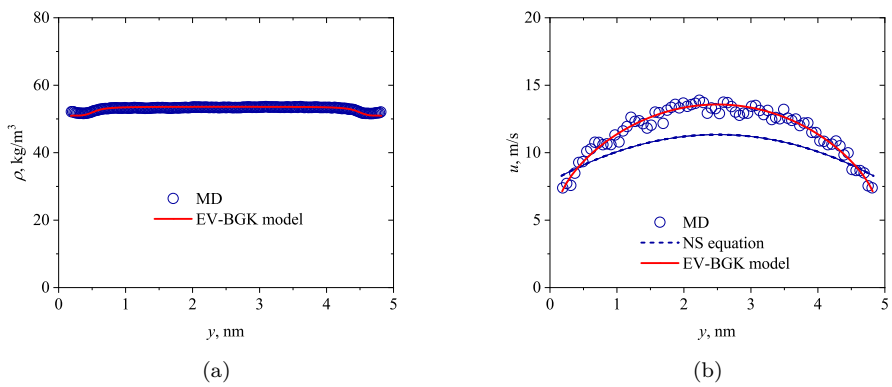

Figure 7 Density (a) and velocity (b) distributions of fluid flows in a 5-nm nanochannel with the averaged density $\rho_{avg} = 49.5$ kg/m^3.

where u_s and $(\partial u/\partial n)_s$ represent the velocity and velocity gradient at the boundary; C_1 and C_2 are the first and second-order slip coefficients, respectively, which are chosen to be $C_1 = 1.0$ and $C_2 = 0.5$ as derived from the linearised Boltzmann equation [20]. Although the molecule size is not considered in the conventional continuum theory, we technically use the effective channel size $H_{eff} = H - \sigma$ as an input in the NS equations for comparisons. Since the interactions among fluid molecules are reflected by the transport coefficients (e.g. viscosity and thermal conductivity) at the continuum level, the NS equations become invalid for nano-scale flows where fluid density inhomogeneities arise and the non-equilibrium effect becomes significant. Overall, the velocity distributions agree well with each other at different densities between the EV-BGK model and MD simulations, see Figures 3(b), 4(b) and 5(b), indicating the capability of the EV-BGK model in capturing the real fluid and non-equilibrium effects.

As shown in Figure 5, the simulated density and velocity profiles predicted by the EV-BGK model partly deviate from the MD data at $\rho = 695$ kg/m^3. This is because

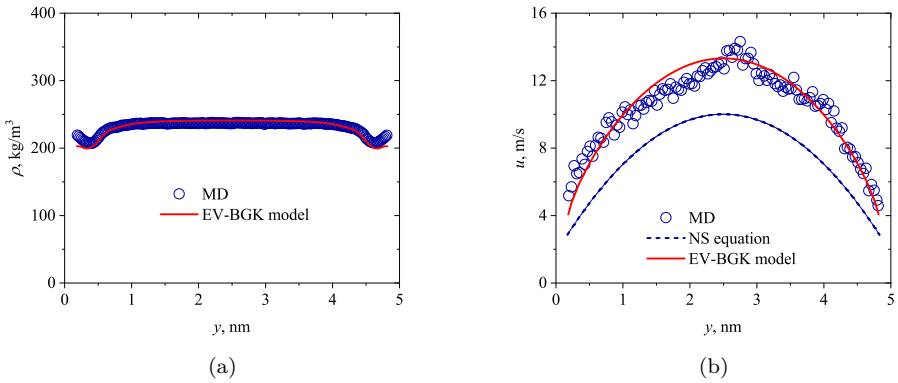

(a) (b)

Figure 8 Density (a) and velocity (b) distributions of fluid flows in a 5-nm nanochannel with the averaged density $\rho_{avg} = 216.0$ kg/m^3.

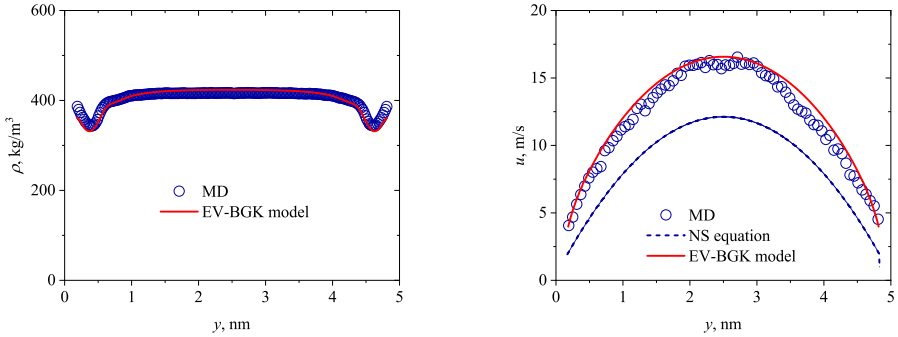

(a) (b)

Figure 9 Density (a) and velocity (b) distributions of fluid flows in a 5-nm nanochannel with the averaged density $\rho_{avg} = 376.0$ kg/m^3.

the EV-BGK model is based on the binary collision assumption, which may not be true for flows at high densities where multiple collisions may become non-negligible.

As the channel size increases to 5 nm, the overall performance of the EV-BGK model is similar to fluid flows in 2-nm channels, see Figures 6∼11. At small densities (i.e. larger Kn), the NS equation overestimates the velocity profiles, see Figure 6(b). When the density increases (i.e. Kn decreases), the non-equilibrium effect becomes weaker, so the NS predictions approach to the EV-BGK model and MD simulations. Within the density range considered in this paper (8.53 kg/m^3 to 695.0 kg/m^3), the EV-BGK model gives satisfactory results compared to the MD simulations.

To better clarify the confinement effect, we extend the channel size to 50 nm, with the density and velocity profiles shown in Figure 12. In this case, the void region near the wall is barely discernible, indicating that the fluid volume exclusion has a negligible effect on the effective channel size. Although there is a slight non-equilibrium effect (Kn=0.01), the NS predictions of velocities are very close to the EV-BGK and MD results. We can infer that as the channel size further increases, the

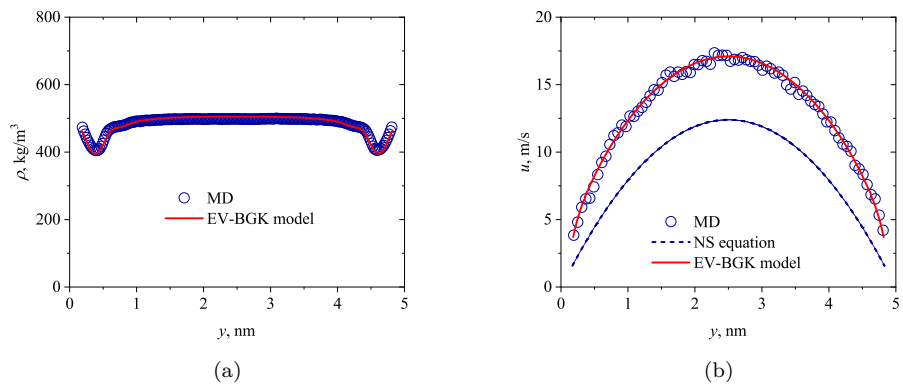

Figure 10 Density (a) and velocity (b) distributions of fluid flows in a 5-nm nanochannel with the averaged density $\rho_{avg} = 450.0$ kg/m^3.

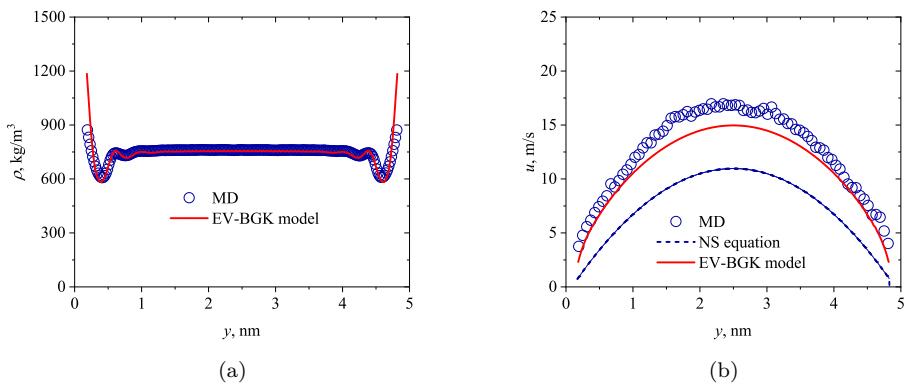

Figure 11 Density (a) and velocity (b) distributions of fluid flows in a 5-nm nanochannel with the averaged density $\rho_{avg} = 695.0$ kg/m^3.

MD (microscopic), EV-BGK model (mesoscopic), and NS equation (macroscopic) will produce the same results as the non-equilibrium, real fluid, and confinement effects become negligible.

3.2 Force distribution across the channel

The real fluid effect manifests itself as the repulsive and attractive forces between fluid molecules on the microscopic level. According to the mean-field and Enskog theories, the attractive and repulsive forces can be approximated by Eqs.(7) and (10), respectively. The distributions of both attractive and repulsive as well as their total forces of Case 9, see Table 1 are shown in Figure 13. Due to the inhomogeneous intermolecular interactions between fluid molecules, the values of these forces change more violently near the wall than in the bulk region, implying the complexities of fluids in the boundary layer. This also directly leads to a more inhomogeneous density distribution adjacent to the wall compared to the bulk region. The total force, which is the microscopic origin of the real fluid effect, is also compared with

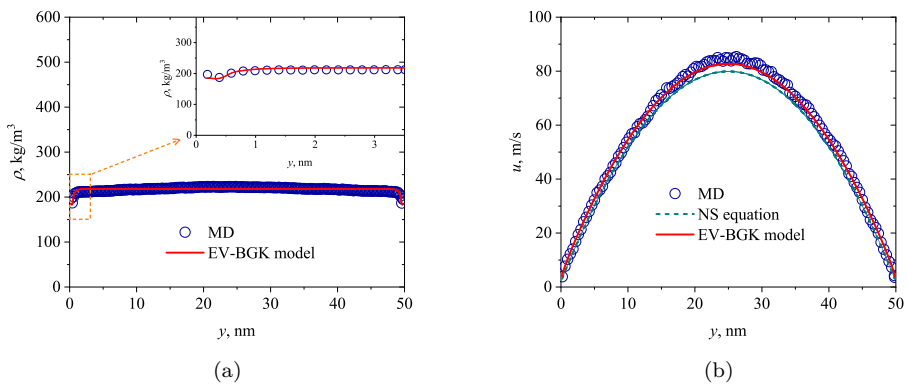

Figure 12 Density (a) and velocity (b) distributions of fluid flows in a 50-nm nanochannel with the averaged density $\rho_{avg} = 216.0$ kg/m^3. The insert is an enlargement of the density distribution near the wall.

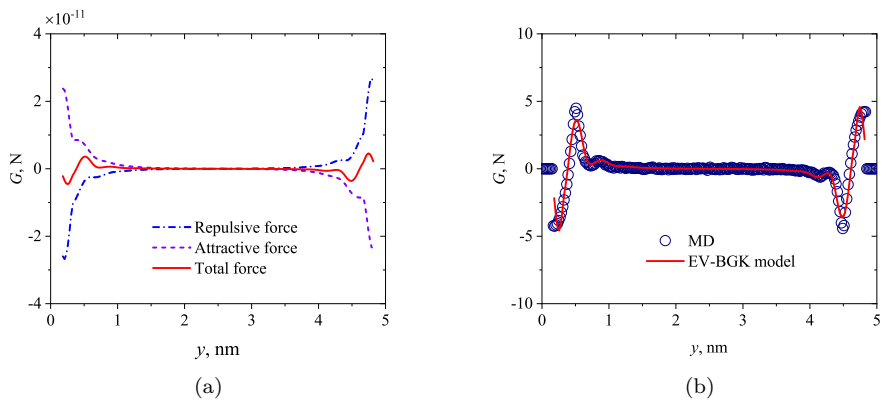

Figure 13 The distribution of attractive, repulsive and total forces among fluid molecules. (a) EV-BGK model results and (b) a comparison of the total forces calculated from the EV-BGK model and MD.

the MD data in Figure 13(b), demonstrating accuracy of the Enskog and mean-filed theories in modelling real fluids.

The total force distribution across the channel directly leads to density inhomogeneities, particularly at high densities. According to the relationship between the force ($\boldsymbol{G}$) and the potential(ϕ), i.e.

$$\boldsymbol{G} = -\frac{\partial \phi}{\partial \boldsymbol{r}}, \tag{27}$$

the intersections between the total force profile and the zero force line correspond to the potential wells, which result in density peaks and valleys, as shown in Figure 14. This further illustrates that the strong real fluid effect may lead to the density inhomogeneity, which is different from the fluid adsorption caused by fluid-solid interactions [48, 49, 50].

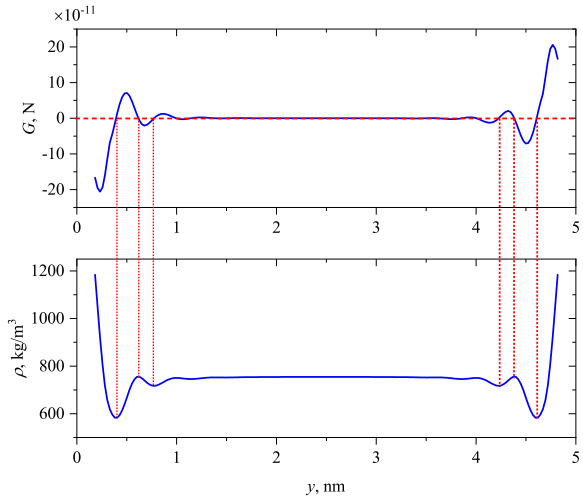

Figure 14 The correlation between the total force and density distributions.

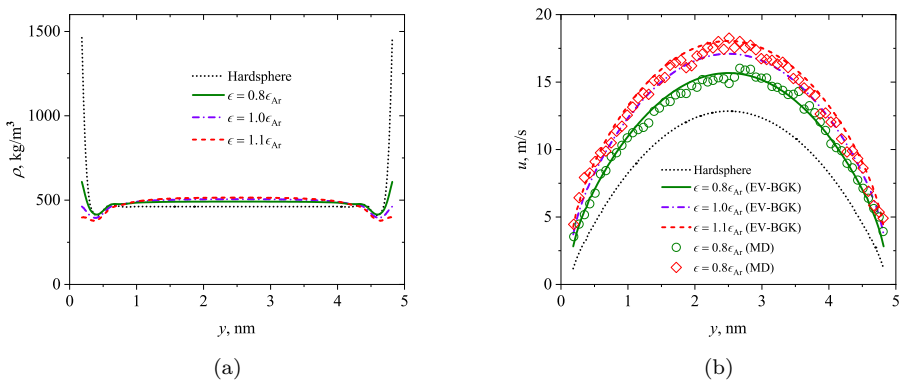

Figure 15 Density (a) and velocity (b) distributions of fluid flows at different fluid attraction strengths.

3.3 Effect of fluid molecular attraction

Real fluid molecules attract each other in the long-range, which is modelled by the attractive potential in Eq. (8) and coupled into the kinetic model through the mean-field force term Ω_{mf} in Eq. (7). The attraction strength is characterised by the energy parameter ϵ. In this part, the energy parameter ϵ is changed to $0.8\epsilon_{Ar}$ and $1.1\epsilon_{Ar}$ to represent weak and strong attraction cases respectively, where ϵ_{Ar} is the energy parameter of Argon used in this study. If the mean-field force term Ω_{mf} is ignored, the EV-BGK model reduces to the Engkog-BGK model, which describes the dynamics of hardsphere fluids, i.e. no attractive forces among fluid molecules. The fluid attraction works as an internal pressure to pull fluid molecules inward into the flow domain, so the fluid density adjacent to the wall becomes smaller as fluid attraction becomes stronger. As shown in Figure 15, the hardsphere fluid density near the wall is the largest as no attraction exists. This straightforward observation can be justified by the equation of state (16), wherein, if the attractive force field (8)

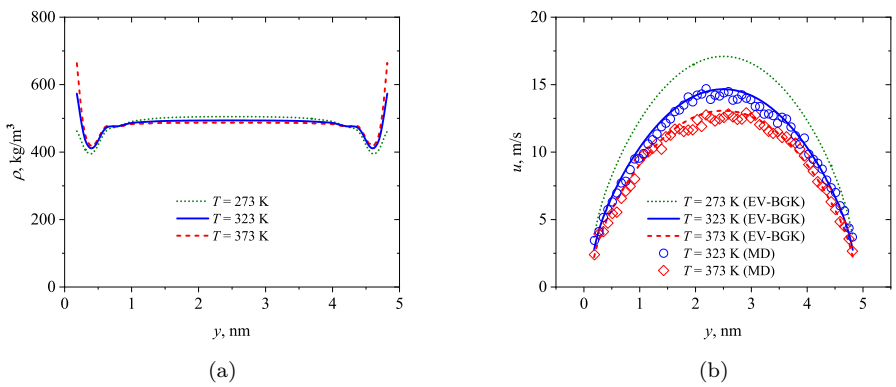

Figure 16 Density (a) and velocity (b) distributions of fluid flows at different temperatures.

is chosen, the attractive contribution to the equilibrium pressure can be written as

$$p^{att} = -\frac{16\pi}{3}\sigma^3 \epsilon n^2. \tag{28}$$

Clearly, the fluid molecular attraction works as an internal negative pressure in fluid equilibrium phase properties. Corresponding to densities at different molecular attractions, the slip velocity increases as fluid molecular attraction becomes stronger. This is because a stronger fluid attraction leads to a smaller fluid density near the wall and thus less efficient momentum exchange between the fluids and the wall.

3.4 Effect of system temperature

The temperature affects density and velocity profiles similar to fluid molecular attractions. At high temperatures, fluid molecules possess more kinetic energy to overcome the attraction from surrounding molecules, hence exhibiting like a weaker attraction among fluid molecules. Consequently, the boundary layer density increases, and the slip velocity decreases with the temperature, as shown in Figure 16. Again, the EV-BGK model produces satisfactory results compared to the MD data.

3.5 Slip velocity of real fluids

The EV-BGK model reduces to the Boltzmann-BGK model when the fluid volume exclusion term Ω_{ex} and the fluid attraction term Ω_{mf} are omitted, which describes the dynamics of ideal fluids. The slip velocities of ideal, hardsphere, and real fluids are shown in Figure 17, which increase with the Kn in all the cases, i.e. a stronger non-equilibrium effect at a larger Kn. The slip velocities of hardsphere and real fluids tend to be the same as the Kn increases, indicating that fluid attraction plays a negligible role at large Kn. With the increase of the channel size, real fluid dynamics approaches to ideal ones as the confinement and real fluid effects become less important.

To evaluate the role of confinement and real fluid effects, the variation of non-dimensional slip velocity with Kn is measured as shown in Figure 17(b), where the slip velocity is normalised by $u_r = \sqrt{2k_BT/m}$. The non-dimensional slip velocity

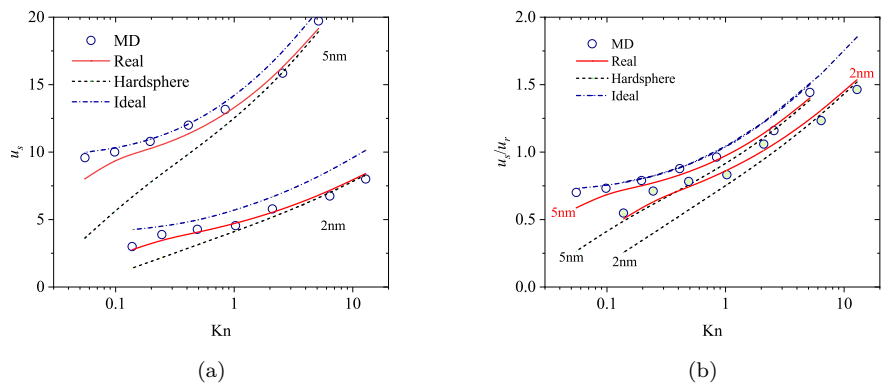

Figure 17 Variation of slip velocity (a) and non-dimensional slip velocity (b) with the Kn.

of the ideal gas coincides for flows at different channel sizes (2 nm and 5 nm), indicating that ideal gas flows are characterised solely by Kn. The non-dimensional slip velocity is different for hard-sphere and real fluids at different confinements, indicating that both confinement and real fluid effects play their roles. This is similar to the disappearance of the Knudsen minimum for dense gases under confinements observed in previous studies [6, 8]. Therefore, fluid flows under confinements are controlled by both confinement and real fluid effects.

4 Conclusions

In this paper, the force-driven Poiseuille flows of real fluids at the nanoscale are investigated by the EV-BGK model at different non-equilibrium and confinement conditions. The simulated results are validated by the MD simulation data. The effects of fluid attraction and system temperature on fluid flows are also analysed. From this study, the following conclusions can be drawn:

(1) The EV-BGK model produces satisfactory density and velocity profiles for real fluid flows within the density range from 8.5 kg/m^3 to 695.0 kg/m^3, which shows its capability in capturing the real fluid effect at large densities and the non-equilibrium effect at large Kn.

(2) Due to the force imbalance caused by the real fluid effect, fluid density exhibits inhomogeneities in nano-scale flows, which is more significant close to the surface as a consequence of more inhomogeneous intermolecular interactions between fluid molecules.

(3) The fluid attraction pulls fluid molecules inward into the flow domain and makes the density distribution less inhomogeneous compared to the hardsphere cases. Therefore, the fluid density in boundary layers will be overestimated, and the slip velocity will be underestimated for real fluids if the long-range attraction is ignored.

This study shows the potential of applying the EV-BGK model in more complicated cases where fluid molecular interactions are more important, such as the liquid-vapour phase transitions [51] and two-phase flows in porous media [52].

Acknowledgements

This paper is dedicated to Dr. Peng Wang, an eminent young scholar and a genuine friend to all of us. He brought many excellent ideas to the research community, including but not limited to the heat transfer of three-dimensional turbulent natural convection flow where he established a novel correlation between the Nusselt number and the Rayleigh number up to 10^{10}, the rarefied gas flows in all flow regimes based on the DUGKS where he revealed that the damping force and heat flow can be controlled by changing the aspect ratio of the geometry and the oscillating frequency of the moving part in micro-devices, and the multiscale modelling where he widened the applicable scope of traditional CFD by incorporating the non-equilibrium effect into the constitutive equation and boundary condition. His work on the kinetic model of the Enskog equation paves the way for the study of non-equilibrium dynamics of dense gases, which is key to understanding the transport of dense gases. This paper is in memory of him for his contribution to this research line.

Funding

This work is supported by the UK's Engineering and Physical Sciences Research Council under grant no. EP/R041938/1 and the National Natural Science Foundation of China under grant no. 51836003 and no. 12002130. Supercomputing time on ARCHER is provided by the "UK Consortium on Mesoscale Engineering Sciences (UKCOMES)" under the UK Engineering and Physical Sciences Research Council Grant No. EP/R029598/1. This work made use of computational support by CoSeC, the Computational Science Centre for Research Communities, through UKCOMES.

Availability of data and materials

The data that support the findings of this study are available from the corresponding author upon reasonable request.

Competing interests

The authors declare that they have no competing interests.

Authors' contributions

Baochao Shan: Methodology, Software, Validation, Formal analysis, Data Curation, Writing - Original draft preparation. Long Ju: Methodology, Writing - Review & Editing. Wei Su: Methodology, Writing - Review & Editing. Zhaoli Guo:Supervision, Funding acquisition, Writing - Review & Editing. Yonghao Zhang: Supervision, Project administration, Funding acquisition, Conceptualization, Writing - Reviewing and Editing.

Author details

[1]School of Engineering, The University of Edinburgh, Edinburgh, UK. [2]Yantai Research Institute, Harbin Engineering University, Yantai, China. [3]Division of Emerging Interdisciplinary Areas, The Hong Kong University of Science and Technology, Hong Kong, China. [4]Institute of Interdisciplinary Research for Mathematics and Applied Science, Huazhong University of Science and Technology, Wuhan, China. [5]Institute of Mechanics, Chinese Academy of Sciences, Beijing, China.

References

1. Shan, B., Ju, L., Guo, Z., Zhang, Y.: Investigation of shale gas flows under confinement using a self-consistent multiscale approach. Advances in Geo-Energy Research **6**(6) (2022)
2. Travis, K.P., Todd, B., Evans, D.J.: Departure from navier-stokes hydrodynamics in confined liquids. Physical Review E **55**(4), 4288 (1997)
3. Wang, F., Qian, J., Fan, J., Li, J., Xu, H., Wu, H.: Molecular transport under extreme confinement. Science China Physics, Mechanics & Astronomy **65**(6), 1–10 (2022)
4. Yu, H., Xu, H., Xia, J., Fan, J., Wang, F., Wu, H.: Nanoconfined transport characteristic of methane in organic shale nanopores: the applicability of the continuous model. Energy & Fuels **34**(8), 9552–9562 (2020)
5. Guo, Z., Zhao, T., Shi, Y.: Generalized hydrodynamic model for fluid flows: From nanoscale to macroscale. Physics of fluids **18**(6), 067107 (2006)
6. Wu, L., Liu, H., Reese, J.M., Zhang, Y.: Non-equilibrium dynamics of dense gas under tight confinement. Journal of Fluid Mechanics **794**, 252–266 (2016)
7. Wang, P., Wu, L., Ho, M.T., Li, J., Li, Z.-H., Zhang, Y.: The kinetic shakhov–enskog model for non-equilibrium flow of dense gases. Journal of Fluid Mechanics **883** (2020)
8. Corral-Casas, C., Li, J., Borg, M.K., Gibelli, L.: Knudsen minimum disappearance in molecular-confined flows. Journal of Fluid Mechanics **945** (2022)
9. Martinez-Val, R., Perez, E.: Aeronautics and astronautics: recent progress and future trends. Proceedings of the Institution of Mechanical Engineers, Part C: Journal of Mechanical Engineering Science **223**(12), 2767–2820 (2009)
10. Lyshevski, S.E.: Nano-and Micro-electromechanical Systems: Fundamentals of Nano-and Microengineering. CRC press, ??? (2018)
11. Su, W., Zhu, L., Wang, P., Zhang, Y., Wu, L.: Can we find steady-state solutions to multiscale rarefied gas flows within dozens of iterations? Journal of Computational Physics **407**, 109245 (2020)
12. Varoutis, S., Valougeorgis, D., Sazhin, O., Sharipov, F.: Rarefied gas flow through short tubes into vacuum. Journal of Vacuum Science & Technology A: Vacuum, Surfaces, and Films **26**(2), 228–238 (2008)
13. Wu, Y., Tahmasebi, P., Lin, C., Munawar, M.J., Cnudde, V.: Effects of micropores on geometric, topological and transport properties of pore systems for low-permeability porous media. Journal of Hydrology **575**, 327–342 (2019)
14. Cai, J., Jin, T., Kou, J., Zou, S., Xiao, J., Meng, Q.: Lucas–washburn equation-based modeling of capillary-driven flow in porous systems. Langmuir **37**(5), 1623–1636 (2021)

15. Luo, S., Ding, C., Cheng, H., Zhang, B., Zhao, Y., Liu, L.: Estimated ultimate recovery prediction of fractured horizontal wells in tight oil reservoirs based on deep neural networks. Advances in Geo-Energy Research **6**(2), 111 (2022)
16. Ju, L., Shan, B., Liu, P., Guo, Z.: Pore-scale study of miscible density-driven mixing flow in porous media. Physics of Fluids **33**(3), 034113 (2021)
17. Wang, Y., Vuik, C., Hajibeygi, H.: Co_2 storage in deep saline aquifers: impacts of fractures on hydrodynamic trapping. International Journal of Greenhouse Gas Control **113**, 103552 (2022)
18. Shan, B., Wang, R., Guo, Z., Wang, P.: Contribution quantification of nanoscale gas transport in shale based on strongly inhomogeneous kinetic model. Energy **228**, 120545 (2021)
19. Gass, D.M.: Enskog theory for a rigid disk fluid. The Journal of Chemical Physics **54**(5), 1898–1902 (1971)
20. Chapman, S., Cowling, T.G.: The Mathematical Theory of Non-uniform Gases: an Account of the Kinetic Theory of Viscosity, Thermal Conduction and Diffusion in Gases. Cambridge university press, ??? (1990)
21. Van Beijeren, H., Ernst, M.H.: The modified enskog equation. Physica **68**(3), 437–456 (1973)
22. Hoffman, D.K., Curtiss, C.: Kinetic theory of dense gases. iii. the generalized enskog equation. The Physics of Fluids **7**(12), 1887–1897 (1964)
23. Hanley, H., McCarty, R., Cohen, E.: Analysis of the transport coefficients for simple dense fluid: Application of the modified enskog theory. Physica **60**(2), 322–356 (1972)
24. Dymond, J.: Corrected enskog theory and the transport coefficients of liquids. The Journal of Chemical Physics **60**(3), 969–973 (1974)
25. Bird, G.A.: Molecular gas dynamics and the direct simulation of gas flows. Molecular gas dynamics and the direct simulation of gas flows (1994)
26. Guo, Z., Zhao, T., Shi, Y.: Simple kinetic model for fluid flows in the nanometer scale. Physical Review E **71**(3), 035301 (2005)
27. Zhang, T., Javadpour, F., Li, X., Wu, K., Li, J., Yin, Y.: Mesoscopic method to study water flow in nanochannels with different wettability. Physical Review E **102**(1), 013306 (2020)
28. Shan, B., Wang, P., Wang, R., Zhang, Y., Guo, Z.: Molecular kinetic modelling of nanoscale slip flow using a continuum approach. Journal of Fluid Mechanics **939** (2022)
29. Enskog, D.: The numerical calculation of phenomena in fairly dense gases. Arkiv Mat. Astr. Fys **16**(1), 1–60 (1921)
30. Vera, J., Prausnitz, J.: Generalized van der waals theory for dense fluids. The Chemical Engineering Journal **3**, 1–13 (1972)
31. He, X., Doolen, G.D.: Thermodynamic foundations of kinetic theory and lattice boltzmann models for multiphase flows. Journal of Statistical Physics **107**(1), 309–328 (2002)
32. Frezzotti, A., Gibelli, L., Lorenzani, S.: Mean field kinetic theory description of evaporation of a fluid into vacuum. Physics of Fluids **17**(1), 012102 (2005)
33. Sadr, M., Gorji, M.H.: Treatment of long-range interactions arising in the enskog–vlasov description of dense fluids. Journal of Computational Physics **378**, 129–142 (2019)
34. Karkheck, J., Stell, G.: Kinetic mean-field theories. The Journal of Chemical Physics **75**(3), 1475–1487 (1981)
35. Benilov, E., Benilov, M.: Energy conservation and h theorem for the enskog-vlasov equation. Physical Review E **97**(6), 062115 (2018)
36. Struchtrup, H., Frezzotti, A.: Twenty-six moment equations for the enskog–vlasov equation. Journal of Fluid Mechanics **940** (2022)
37. Luo, L.-S.: Unified theory of lattice boltzmann models for nonideal gases. Physical review letters **81**(8), 1618 (1998)
38. He, X., Shan, X., Doolen, G.D.: Discrete boltzmann equation model for nonideal gases. Physical Review E **57**(1), 13 (1998)
39. Bhatnagar, P.L., Gross, E.P., Krook, M.: A model for collision processes in gases. i. small amplitude processes in charged and neutral one-component systems. Physical review **94**(3), 511 (1954)
40. Shan, B., Chen, S., Guo, Z., Wang, P.: Pore-scale study of non-ideal gas dynamics under tight confinement considering rarefaction, denseness and molecular interactions. Journal of Natural Gas Science and Engineering **90**, 103916 (2021)
41. Carnahan, N.F., Starling, K.E.: Equation of state for nonattracting rigid spheres. The Journal of chemical physics **51**(2), 635–636 (1969)
42. Tarazona, P.: Free-energy density functional for hard spheres. Physical Review A **31**(4), 2672 (1985)
43. Guo, Z., Xu, K., Wang, R.: Discrete unified gas kinetic scheme for all knudsen number flows: Low-speed isothermal case. Physical Review E **88**(3), 033305 (2013)
44. Guo, Z., Xu, K.: Progress of discrete unified gas-kinetic scheme for multiscale flows. Advances in Aerodynamics **3**(1), 1–42 (2021)
45. Shan, B., Wang, P., Zhang, Y., Guo, Z.: Discrete unified gas kinetic scheme for all knudsen number flows. iv. strongly inhomogeneous fluids. Physical Review E **101**(4), 043303 (2020)
46. Zhang, Y., Zhu, L., Wang, R., Guo, Z.: Discrete unified gas kinetic scheme for all knudsen number flows. iii. binary gas mixtures of maxwell molecules. Physical Review E **97**(5), 053306 (2018)
47. Ju, L., Shan, B., Yang, Z., Guo, Z.: An exact non-equilibrium extrapolation scheme for pressure and velocity boundary conditions with large gradients in the lattice boltzmann method. Computers & Fluids **231**, 105163 (2021)
48. Shen, W., Li, X., Cihan, A., Lu, X., Liu, X.: Experimental and numerical simulation of water adsorption and diffusion in shale gas reservoir rocks. Advances in Geo-Energy Research **3**(2), 165–174 (2019)
49. Zhao, Y., Liu, X., Zhang, L., Shan, B.: A basic model of unconventional gas microscale flow based on the lattice boltzmann method. Petroleum Exploration and Development **48**(1), 179–189 (2021)
50. Zhang, L., Liu, C., Li, Q., Wang, S., Cai, S., Huo, E.: Shale gas transport through the inorganic cylindrical and conical nanopores: A density gradient driven molecular dynamics. International Journal of Heat and Mass Transfer **183**, 122126 (2022)

51. Frezzotti, A., Barbante, P., Gibelli, L.: Direct simulation monte carlo applications to liquid-vapor flows. Physics of Fluids **31**(6), 062103 (2019)
52. Wu, Y., Tahmasebi, P., Liu, K., Fagbemi, S., Lin, C., An, S., Ren, L.: Two-phase flow in heterogeneous porous media: A multiscale digital model approach. International Journal of Heat and Mass Transfer **194**, 123080 (2022)